Ibn Al-Haitham Journal for Pure and Applied Sciences
Journal homepage: jih.uobaghdad.edu.iq
PISSN: 1609-4042, EISSN: 2521-3407
IHJPAS. 2024, 37(3)

Synthesis, Characterization of Nickel Cobaltite Nanoparticles and Its Use in Removal Methyl Green Dye from Aqueous Solution

Maryam Abdulsatar Abduljabar[1*] and **Sundus Hadi Merza**[2]
[1,2]Department of Chemistry, College of Education for Pure Science (Ibn Al-Haitham), University of Baghdad, Baghdad, Iraq.
*Corresponding Author.

Received: 11 April 2023 Accepted: 23 May 2023 Published: 20 July 2024
doi.org/10.30526/37.3.3398

Abstract

In this study, nickel cobaltite (NC) nanoparticles were created using the sol-gel process and used as an adsorbent to adsorb methyl green dye (MG) from aqueous solutions. The adequate preparation of nickel cobaltite nanoparticles was verified using FT-IR, SEM, and X-ray diffraction (XRD) studies. The crystalline particle size of NC nanoparticles was 10.53 nm. The effects of a number of experimental variables, such as temperature, adsorbent dosage, and contact time, were examined. The optimal contact time and adsorbent dosage were 120 minutes and 4.5 mg/L, respectively. Four kinetic models—an intraparticle diffusion, a pseudo-first-order equation, a pseudo-second-order equation, and the Boyd equation—were employed to monitor the adsorption process. Modeling of the experimental data showed that the pseudo-second-order model accurately captured the adsorption kinetics due to the high value of the correlation coefficients (R^2). MG dye is gradually adsorbed to the NC nanoparticles through boundary layer diffusion and intraparticle diffusion. The results of the thermodynamic analysis showed that the MG dye adsorption was endothermic and a nonspontaneous phyisorption process.

Keywords: Weber and Morris, boyd model, EDX analysis, percentage removal.

1. Introduction

The presence of dyes in the water stream has a significant impact on daily life. Because dyes are produced in millions of tons globally and utilized in both small- and large-scale industries, such as the leather industry, food industry, cosmetic industry, textile industry, and pharmaceutical industry [1]. Dyes are primarily responsible for the higher mortality rates of kidney, liver, and bladder malignancies. Dyes have complicated structures with aromatic rings linked to various functional groups. Due to their high thermal and chemical stability, many dyes are resistant to degradation by light, heat, and natural oxidants, making dye removal from wastewater extremely important [2,3]. A number of technologies have been employed to remove dyes, such as advanced oxidation [4], biological treatment [5], using natural materials

for biosorption, adsorption on activated carbon, coagulation/flocculation [6], ultrafiltration [7], and reverse osmosis [8].

Most of these technologies are very expensive. In particular, nanotechnology presents a promising method for the adsorption of dyes from aqueous solutions due to the distinctive physicochemical features

of the nanoparticles, such as high chemical reactivity, conductivity, magnetic and optical properties, as well as catalytic potential. Nanomaterials have been investigated for the adsorption of various contaminants, metal ions [9, 10], dyes [11–13], and antibiotics [14]. Multiple types of nano adsorbents have been created and are being used to treat wastewater, such as nanoparticles, nanofibers, nano clays, silica nanoparticles, and carbonaceous nanomaterials.

In recent years, low-cost and nontoxic [15] nanoparticles, particularly metallic and bimetallic oxides, have been employed to eliminate contaminants. Nickel cobaltite (NC) in a spinel structure, AB2O4, is one of the essential bimetallic oxides.

In comparison to a single metal element, bimetallic oxides demonstrated better adsorption performance [16]. In this study, NC was prepared and characterized using FT-IR, XRD, SEM, and EDX analysis. NC is used as an adsorbent to remove methyl green (MG) dye from an aqueous solution. MG is a cationic triphenylmethane that is frequently used in biology and medicine to modify the color of solutions as well as as a photochromophore to ignite coagulated films [17]. The MG molecular structure is depicted in **Figure 1**. The kinetic and thermodynamic characteristics, as well as factors like temperature and adsorbent dosage that affect adsorption, were taken into consideration when carrying out the study.

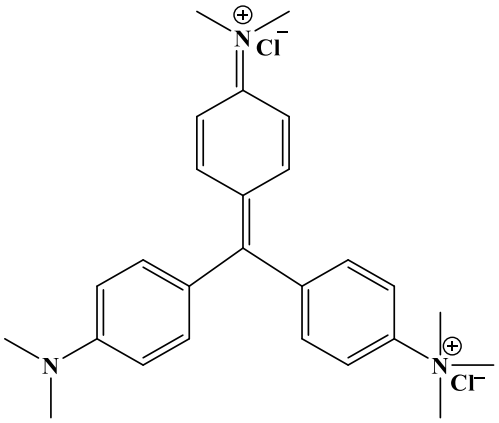

Figure 1. Methyl green dye structure

2. Materials and Methods

2.1 Chemicals and Materials

Methyl green (MG) dye with a maximum wavelength (λ max =618 nm), chemical formula $C_{26}H_{33}Cl_2N_3$ and molecular weight of 458.47 mole/L were provided by WINLAB LIMITED-UNITED KINGDOM and utilized without further purification. BDH supplied $Co(NO_3)_2$•$6H_2O$ and Ni(NO3)2•6 H_2O. The NaOH was purchased from the GCC Company.

2.2 Characterization methods

The average size of the NC was studied using an X-ray powder diffractometer (XRD), 6000 Shimadzu (Japan), using Cu (1.54060), voltage: 40.0 kV, and current: 30.0 mA. Shimadzu 8400s (Japan) spectrophotometers were used to study the characteristics of functional groups.

Moreover, scanning electron microscopy (SEM) and energy dispersive X-ray (EDX) techniques (MIRA3 TESCAN, Czech) were used to examine the morphology and chemical components of NC adsorbent.

2.3 Preparation of nickel cobaltite

Nickel cobaltite (NC) was synthesized following the procedure outlined by Imranullah et al. with some modifications [18]. About 0.1 M Co $(NO_3)_2.6H_2O$ and 0.1 M Ni $(NO_3)_2.6H2O$ were mixed using a magnetic stirring hotplate to form a pink solution. When the temperature reached 50–60 °C, a solution of NaOH (50 mL) was added gradually using a separating funnel (pH around 9–10). The color of the solution gradually changed from dark red to blue and finally to green. The gel form was obtained after the addition of NaOH was completed. The gel was washed several times with water and ethanol using a centrifuge and finally dried at 100 °C for 2 hours. The NC nanoparticles were obtained after calcining the dried sample at 300 °C for 2 hours..

2.4 Adsorption Experimental

Prior to the adsorption procedure, standard solutions in the range of 1–15 mg/L were prepared daily by serial dilution from the MG stock solution, which was prepared by dissolving 0.1 g in 1000 ml of distilled water. The maximum absorption was assessed using a UV-visible spectrophotometer (Shimadzu 1800, Japan). The calibration curve was created using the Beer-Lambert law by plotting the absorption results against the standard dye solution concentration. The determined slope served as a guide for determining concentration in the remaining experiments. **Figure 2** displays the calibration curve.

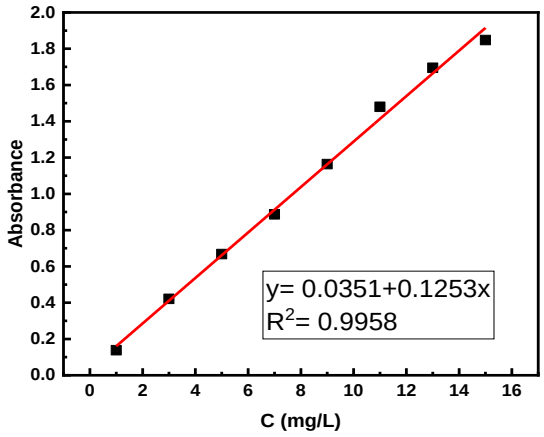

Figure 2. Calibration curve of MG dye solution.

Equation 1 was used to calculate the MG dye adsorption capacity at time t (mg/g) [19].

$$q_t = \frac{(c_\circ - c_t)V}{m} \qquad (1)$$

Where c° (mg/L) and ct(mg/L) are the initial MG concentrations and the concentration of the MG dye solution at t time, respectively. The volume of the MG solution is V (L), and the weight of the NG adsorbent is m (g). The removal efficiency (R%) of MG was estimated using Eq 2.

$$R = \frac{(C_\circ - C_t)}{c_\circ} \times 100 \qquad (2)$$

3. Results and Discussion

3.1 Characterization of NC

3.1.1 The XRD analysis

The X-ray pattern of NC nanoparticles is presented in **Figure 3**. It has been found that NC has a crystalline structure. The XRD diffractogram of $NiCo_2O_4$ exhibits Bragg reflection peaks at 2θ=19.145°, 31.261°, 36.849°, 44.792°, 55.066°, 59.231°, and 65.022°. All Bragg peaks are in good agreement with the Joint Committee on Powder Diffraction Standards (JCPDS) (card no. 073-1702)[20]. **Table 1** lists the interplanar spacing (d) and diffraction peak positions (2θ) of the prepared $NiCo_2O_4$ and the JCPDS. The matching in (d) and the small displacement change in (2θ) support the production of NC. Using Debye-Scherer Equation 3[21], the average crystallite size (d) of the $NiCo_2O_4$ particles was computed.

$$d = (0.94\,\lambda)/(\beta_D \cos\theta) \qquad (3)$$

Where β_D is the diffraction peak's full width at half maximum (FWHM) in radians, θ is the Bragg diffraction angle peak, and λ is the X-ray wavelength of Cu-K =0.1542 nm. The calculated average crystallite size is 10.53 nm. The broad peaks and low intensity support the crystalline grain's modest size.

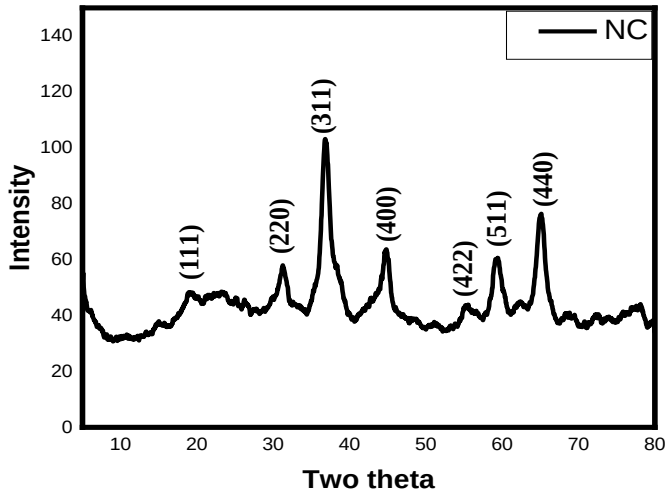

Figure 3. The XRD diffractogram of NC nanoparticles**.**

The lattice constant (unit cell dimension) of the spinel structure NC crystal was calculated using the cubic lattice formula.

$$a = \sqrt{h^2 + k^2 + l^2} \qquad (4)$$

Where the Miller indices are h, k, and l. The computed value of (a) is tabulated in **Table 1**. The values of a are quite similar to the $NiCo_2O_4$ provided in the JCPDS 20-0781 file [22].

Table 1. Compares $NiCo_2O_4$ diffraction peak positions and interplanar spacing (d) with JCPDS (card no. 073-1702 and 00-020-0781).

	(2θ) degree		(d) spacing		
Mille index	**$NiCo_2O_4$ prepared**	**JCPDS (073-1702)**	**$NiCo_2O_4$ prepared**	**JCPDS (073-1702)**	**Lattice constant**
(111)[a]	19.145°	18.928°	4.63	-	8.019
(220)	31.261°	31.152°	2.85	2.87	8.06
(311)	36.849°	36.705°	2.43	2.45	8.059
(400)	44.792°	44.635°	2.02	2.03	8.08
(422)[b]	55.066°	44.635°	1.65	-	8.083
(511)	59.231°	59.115°	1.55	1.56	7.79
(440)	65.022°	64.963°	1.43	1.43	8.089
a (4.69) b (1.65) JCPDS (card no.) 00-020- 0781[23]					

3.1.2 The FT-IR analysis

The $NiCo_2O_4$ exhibits a wide band in its spectra between 2500 and 3500 cm^{-1}, which is caused by O-H stretching [24]. The H-O-H bending vibration mode is indicated by the bands between 1300 cm^{-1} and 1500 cm^{-1} . The bands between 520 cm^{-1} and 650 cm^{-1} were attributed to the stretching vibration of the Ni–O and Co–O [21].

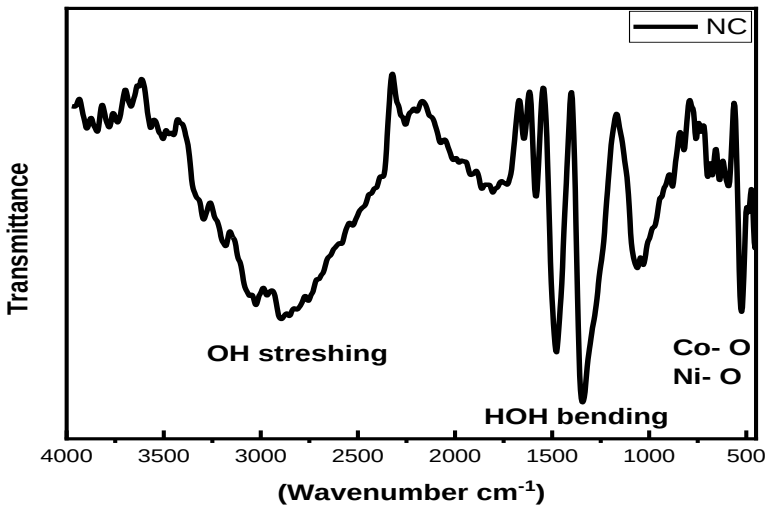

Figure 4. The FT-IR spectrum of NC nanoparticles.

3.1.3 SEM analysis

The main controlling parameters to obtain various NC structures are solvents, reaction time, and temperature [25]. **Figure 5** depicts the SEM image of NC prepared using distilled water and calcined at 300 °C for 2 hours at 135 kx and 5.00 kx magnification. The NC-prepared images showed the growth of nanorods as well as aggregated nanoparticles as plates. The EDX analysis of NC nanoparticles confirms that there are no foreign elements in the sample.

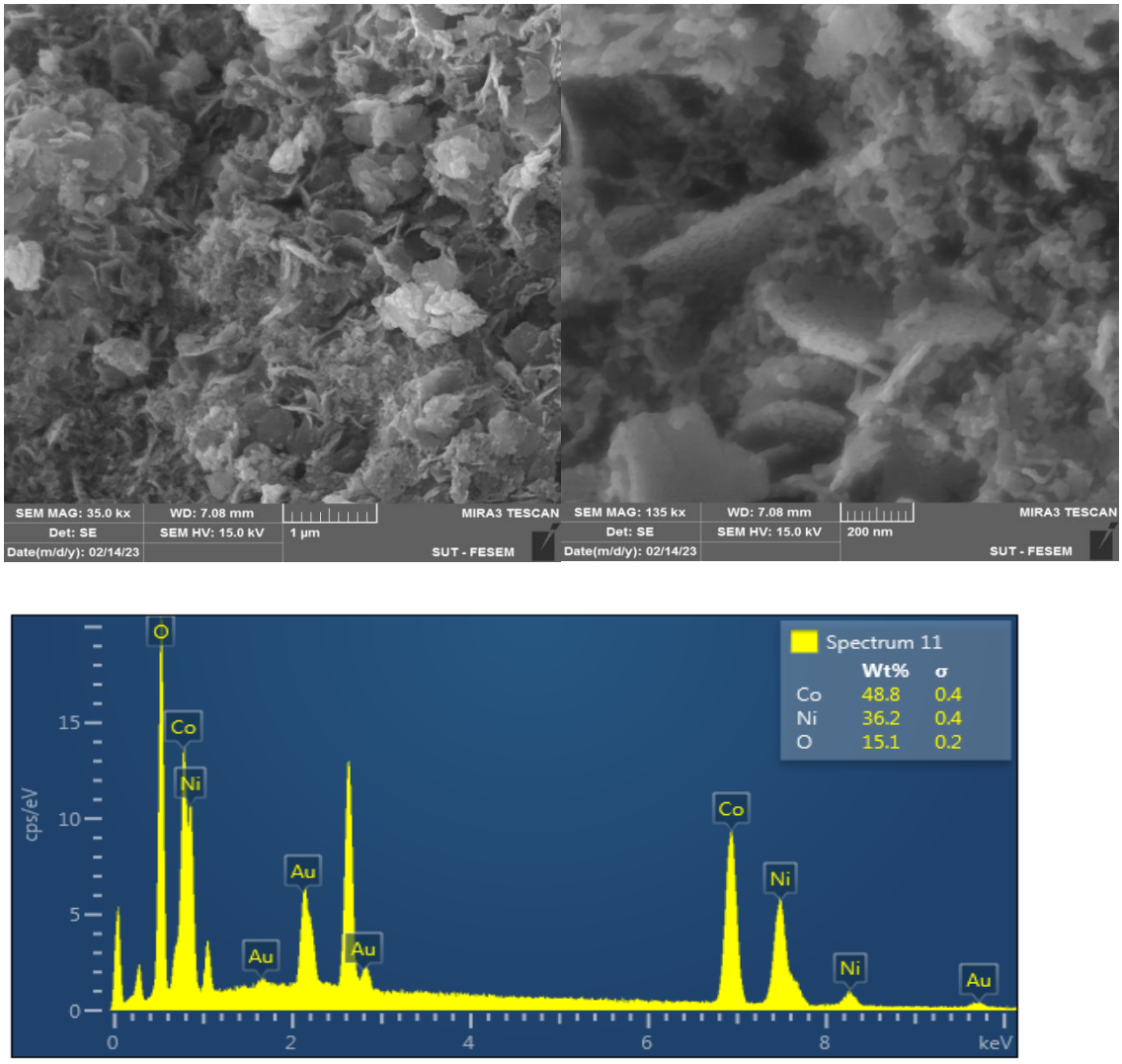

Figure 5. The SEM image and EDX analysis of NC nanoparticles.

3.2 Effects of temperature, contact time and dosage on MG removal

The impact of contact time and temperature on the percentage removal of MG using NC adsorbent is clearly shown in **Figure 6**. The adsorption achieved equilibrium within 100 minutes and continued after this point. This can be explained by the fact that at the beginning of the adsorption process, there were a lot of empty active adsorption sites on the surface of the NC. As the contact time increased, the active adsorption sites were gradually occupied and diminished. The optimal contact time for MG is 120 minutes. The effect of temperature on the adsorption percentage of MG dye from solution on NC adsorbent was determined at different temperatures of 288 K, 298 K, and 308 K. As seen in **Figure 6**, the adsorption percentage increased significantly from 27.59% at 288 K to 56.37% at 308 K. The enhanced interactions between the empty spaces on the adsorbent surface and the MG dye molecules, as well as the increased molecular mobility of the dye molecules, are likely the causes of the preferred removal of MG dye with temperature increases. It is also evident that as the temperature rises, the removal percentage rises as well [26]. The outcomes of the experiment show that the adsorption of MG onto the NC adsorbent is an endothermic process.

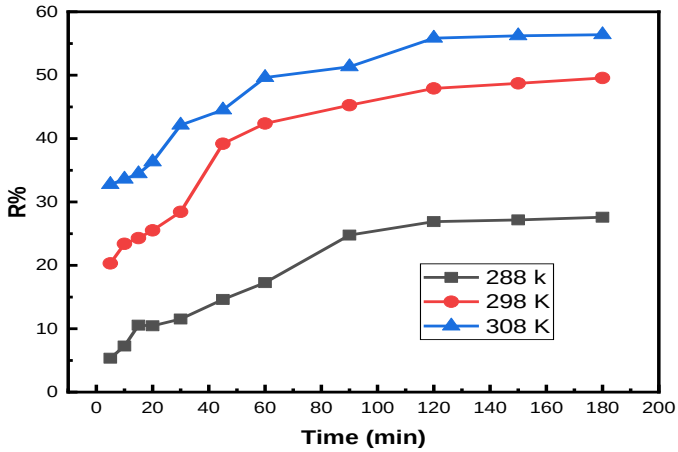

Figure 6. Effect of temperature and contact time on MG removal.

With a set starting concentration of 15 mg/L and a constant temperature of 298 K, the adsorption of MG on the NC was tested with different dosages of adsorbent ranging from 0.001 g to 0.005 g. The initial dye removal percentage increased as the adsorbent dosage increased, as shown in **Figure 7**. This may be attributed to the increased surface area and the unoccupied dye-binding sites on the adsorbent surface. The saturation of the free active sites by MG dye caused a modest increase in the removal percentage. The optimal adsorbent dosage for future adsorption investigations was found to be 0.0045 g.

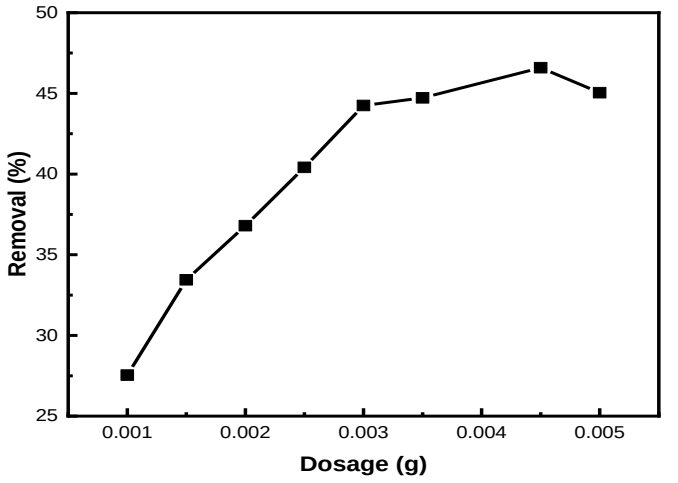

Figure 7. Effect of adsorbent dosage on percentage removal of MG dye.

3.3 Adsorption kinetics study

To characterize the kinetics of pollutants (MG dye), the movement of the adsorbate within and onto the surface sites of the adsorbent, and possible rate-limiting steps, a variety of adsorption kinetic models such as pseudo-first-order (PFO), pseudo-second-order (PSO), Weber's intraparticle diffusion, and Boyd have been used [27–29]. Equations 5 and 6 define the linearized forms of the PFO and PSO models, respectively.

$$\ln(q_e - q_t) = \ln q_e - k_1 t \quad (5)$$

$$\frac{t}{q_t} = \frac{1}{k_2 q_e^2} + \frac{t}{q_e} \quad (6)$$

The slope and intercept of the ln (qe-qt) vs. time plot can be used to calculate the rate constant k_1 (1/min) and the amount of MG absorbed at equilibrium (q_e) (mg/g). The weight of the adsorption capacity of MG absorbed at the time (t) in minutes is represented by the q_t (mg/g). The rate constant of the second order, k_2(g/mg. min), was determined from the intercept of the plot of t/q_t vs. t. **Table 2** displays the PFO and PSO kinetic parameters.

Table 2. Modeling coefficients for the kinetic adsorption of PFO and PSO (MG = 15 mg/L, NC = 3 mg/L).

	Temperature		
Pseudo-first order model	**288**	**298**	**308**
$q_{e,\,exp}$ (mg/g)	9.19	16.52	18.79
$q_{e,\,cal}$ (mg/g)	19.90	12.11	9.01
K_1(1/min)	-0.0286	-0.0252	-0.0229
SSE	1.183	0.1173	1.565
R^2	0.9576	0.9854	0.7019
Pseudo-second order model			
$q_{e,\,cal}$ (mg/g)	11.54	18.08	19.84
K_2(g/mg· min)	0.00196	0.00317	0.00477
SSE	1.070	0.692	0.271
R^2	0.9627	0.9939	0.9971

Table 2 clearly shows that the correlation coefficient R^2 of PFO kinetics is lower than that of PSO and that the computed qe (mg/g) values do not closely match the experimental qe (mg/g) values. Also, the value of the sum of squares error (SSE) is higher than the PSO. Therefore, it can be inferred that the PFO kinetic model **Figure 8** is inappropriate for predicting the adsorption kinetics of MG dye onto NC adsorbent. The PSO model accurately predicts the adsorption process with a higher R^2 value, as shown in **Figure 8**. This implies that the chemical process was in control of the adsorption process. Similar behavior has been seen in the adsorption of MG by multi-walled carbon nanotubes decorated with nickel nano ferrite adsorbent and graphene sheet adsorbent [30, 31].

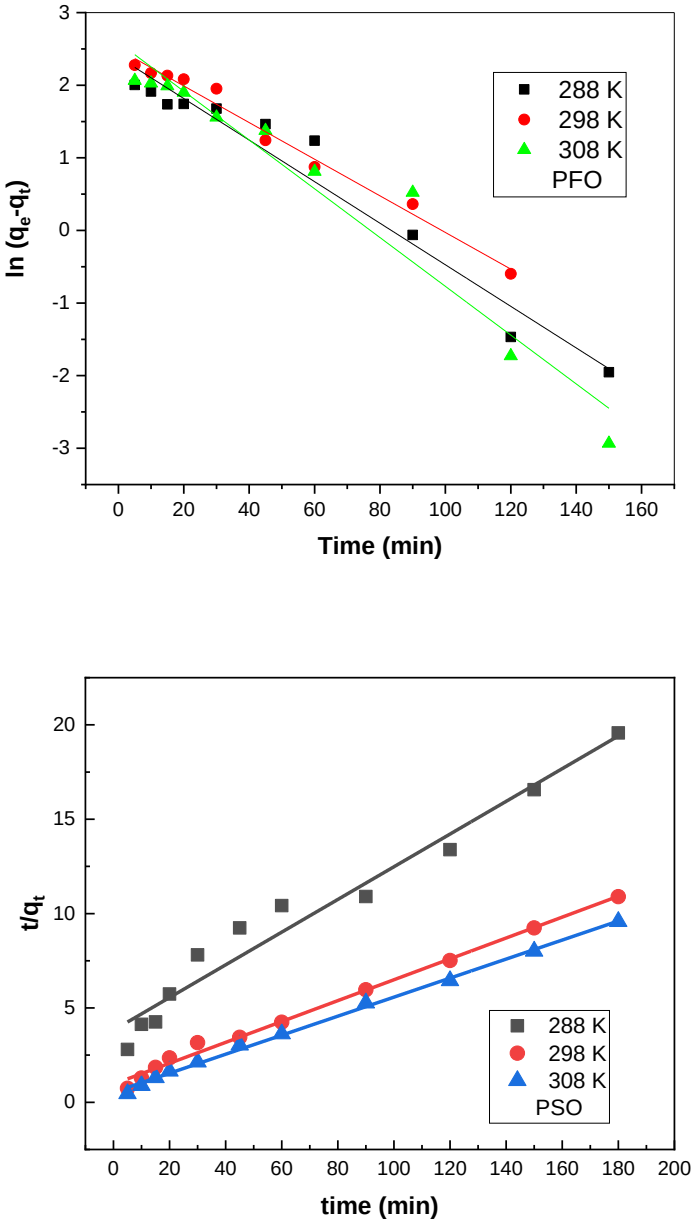

Figure 8. The PFO and PSO models for MG dye on NC adsorbent at different temperatures.

In order to forecast the rate-controlling diffusion mechanism within the adsorption system, the Weber and Morris intraparticle diffusion and Boyd models were applied. The linearized form of the Weber and Morris model is shown in **Eq 7**.

$$q_t = k_d t^{0.5} + c \qquad (7)$$

Where the slope and intercept of the qt against the t0.5 plot can be used to get the diffusion rate constant, kd (mg/g.min-0.5), and the boundary layer thickness constant, c (mg/g). The plots of intra-particle diffusion are depicted in **Figure 9**. The plot of the entire process consists of three linear plots rather than a single line. The kinetic variables with the regression coefficient R2 for each step are presented in **Table 3**. The first step is assigned to external diffusion. In this step, the adsorbate penetrates the liquid film surrounding the adsorbent. The concentration difference between the bulk solution and the adsorbent's surface acts as the driving force of external

diffusion. The low driving force may be the cause of the low k value [32]. The second stage is focused on adsorbate diffusion and adsorption within the pores and active sites of the adsorbent. The high value of kd demonstrates the high adsorption rate and verifies the existence of many active sites. The third step shows the equilibrium in the adsorption process. The kd values have minimum values due to the low MG dye concentration remaining in the solution and the saturation of the pores and active sites of the adsorbent. On the other hand, boundary diffusion (C) values increased as temperature rose, indicating that surface adsorption became more prominent [33]. According to the adsorption data, the process of MG dye removal from an aqueous solution is complicated and involves both boundary layer diffusion and intra-particle diffusion.

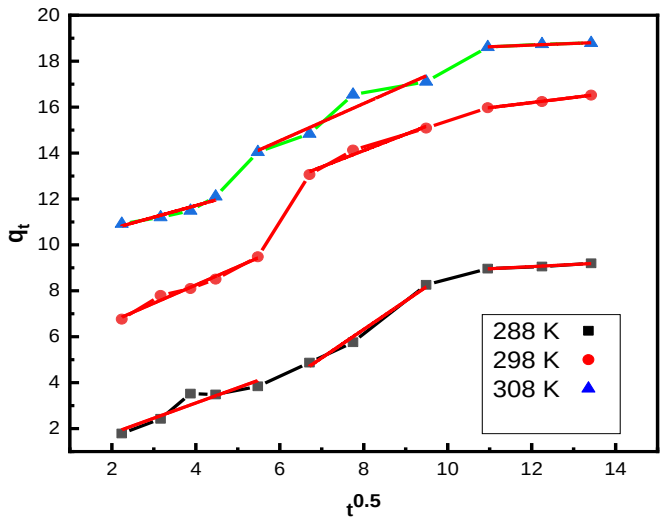

Figure 9. Weber and Morris intraparticle diffusion.

Table 3. Parameters for intra-particle diffusion based on three steps.

	Step 1			Step 2			Step 3		
T/ K	Kd (mg.g^{-1}. min$^{-0.5}$)	C (mg/g)	R^2	Kd (mg.g^{-1}. min$^{-0.5}$)	C (mg/g)	R^2	Kd (mg.g^{-1}. min$^{-0.5}$)	C (mg/g)	R^2
288	0.6615	0.4685	0.9162	1.2415	-3.6134	0.9848	0.9321	7.9356	0.9741
298	0.7095	5.0737	0.9818	0.790	8.4322	0.9695	0.2230	13.5222	0.9977
308	0.5043	9.6947	0.9127	0.8106	9.6693	0.9203	0.0724	17.8309	0.9613

The Boyd equation [34]was used to forecast the regulating mechanism for MG adsorption on NC adsorbent. It is stated as following equation

$$-\ln(1-F) = k_b t \qquad (8)$$

F is determined as q_t/q_e, and the Boyd constant is k_b (min^{-1}). According to the Boyd equation (linear behavior, zero intercept value), the diffusion of adsorbate in a bounded liquid layer around the adsorbent is the slowest process; otherwise, film diffusion and pore diffusion regulate the adsorption mechanism. As can be observed from **Figure 10**, linear behavior with a zero value of intercept is not reported, highlighting the significance of both film diffusion and pore diffusion as the governing processes for the mechanism of MG adsorption onto NC. Thus,

it was found that there were multiple steps involved in the adsorption mechanism of MG onto NC.

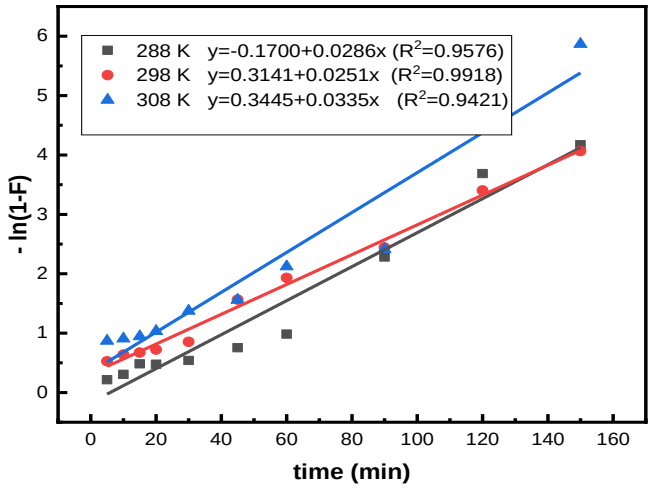

Figure 10. Boyd model for MG adsorption on NC nanoparticles

3.4 Activation energy and thermodynamic parameters

The Arrhenius relationship is used to express the pseudo-second-order rate constant k_2 of dye adsorption as a function of temperature. [35]:

$$\ln k_2 = \ln A - \frac{E_a}{RT} \quad (9)$$

Where R and T are the gas constant (8.314 J/mol K) and T is the absolute temperature, E_a is the Arrhenius activation energy of adsorption, and A is the Arrhenius factor. A straight line with a slope of $-E_a/R$ is produced when ln k_2 is plotted against 1/T, as shown in **Figure 11**. A value of 32.79 (kJ/mol) was determined as the activation energy. This value indicats that the adsorption has a low potential barrier and relates to a phyisorption process [31, 36].

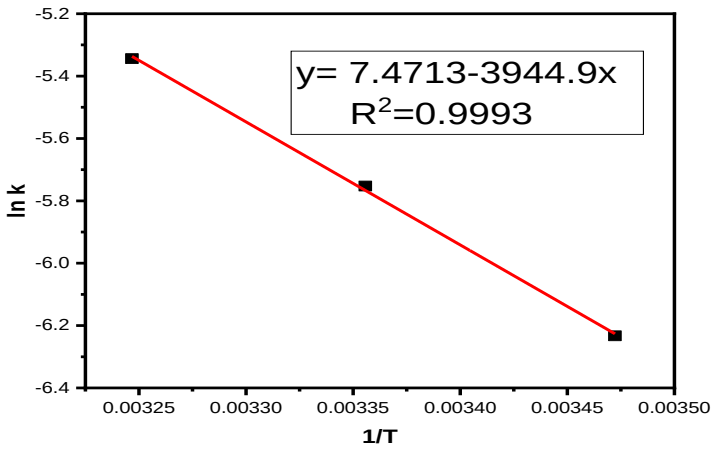

Figure 11. Plot of the activation energy for the MG adsorption on NC nanoparticles.

The Eyring equation was used to calculate the thermodynamic activation parameters of the process, such as enthalpy (H^*), entropy (S^*), and free energy (G*), to demonstrate the impact of solution temperature on the transport/kinetic process of MG dye adsorption [35, 37].

$$ln\frac{k_2}{T} = ln\frac{k_B}{h} + \frac{\Delta S^*}{R} - \frac{\Delta H^*}{RT} \quad (10)$$

Where k_B and h are the Boltzmann constants 1.3807×10^{-23} (J/K) and the Planck constant 6.6261×10^{-34} (J s), respectively. k_2 is the PSO rate constant. When plotting $\ln(k_2/T)$ against 1/T, a straight line should be drawn. The slope ($-\Delta H^*/R$) and intercept ($\ln k_B/h + \Delta S^*/R$) of the line were used to determine the ΔH^* and ΔS^* **Figure 12**. The activation enthalpy change value (30.32 kJ/mol) indicates that the adsorption is endothermic in nature. A negative value of ΔS^* (191.09 J/mole) indicates the presence of an associative mechanism in the adsorption process. The free energy of activation (ΔG^*) for the adsorption of MG onto NC was calculated using Equation. 11.

$$\Delta G^* = \Delta H^* - T\Delta S^* \quad (11)$$

The free energies were calculated to be 85.35, 87.27, and 89.18 at 288, 298, and 308 K, respectively. The fact that the positive values of Gibbs free energy of the MG adsorption at all temperatures suggest a non-spontaneous process. Similar behaviors have already been reported in other research [35, 38].

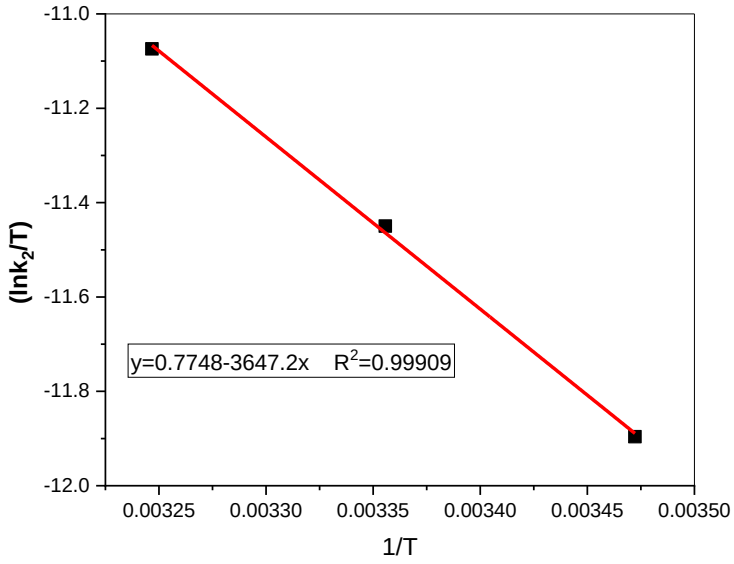

Figure 12. Plot of $\ln K_2/T$ versus 1/T.

4. Conclusion

The SEM-EDX, XDR, and FT-IR analyses confirmed the formation of NC. The adsorption of MG dye onto NC nanoparticles was investigated under optimum conditions. The fitness of the experimental data was assessed using PFO and PSO kinetic models. The PSO reaction model is a good fit for the MG dye's adsorption kinetics. The computed qe values from the PSO model were in good agreement with the experimental findings. The results of the adsorption of

MG onto NC showed that adsorbent dosage and temperature influenced the adsorption and removal of the adsorbent. The percentage removal of MG dye increased with an increase in the dosage of the adsorbent. At 308 K, the highest percentage removal of 56.37% was observed. According to the kinetic studies, equilibrium in the MG adsorption on NC was reached after 120 minutes. The results indicated that both film diffusion and intraparticle diffusion are involved in the mechanism of adsorption, in accordance with the Weber and Morris equation and Boyd plot. The adsorption of MG is a phyisorption process that is non-spontaneous and endothermic.

Acknowledgment

The authors the Department of Chemistry, College of Education for Pure Science (Ibn Al-Haitham), University of Baghdad, for facilitating the work of the practice in this article.

Conflict of Interest

The authors declare that they have no conflicts of interest

Funding

There is no financial support.

References

1. Hassaan, M.; Nemr, A. El; Hassaan, M.A. Health and Environmental Impacts of Dyes: Mini Review. *American Journal of Environmental Science and Engineering*. **2017**, *1(3)*, 64–67. https://doi.org/10.11648/j.ajese.20170103.11.
2. Katheresan, V.; Kansedo, J.; Lau, S. Y. Efficiency of various recent wastewater dye removal methods: A review. *Journal of Environmental Chemical Engineering.* **2018**, *6*(*4*), 4676-4697. https://doi.org/10.1016/j.jece.2018.06.060.
3. Bae, J.S.; Freeman, H.S. Aquatic Toxicity Evaluation of New Direct Dyes to the Daphnia Magna. *Dye and Pigments.* **2007**, *73(1)*, 81–85. https://doi.org/10.1016/j.dyepig.2005.10.015.
4. Othmani, A.; Kesraoui, A.; Akrout, H.; López-Mesas, M.; Seffen, M.; Valiente, M. Use of Alternating Current for Colored Water Purification by Anodic Oxidation with SS/PbO2 and Pb/PbO2 Electrodes. *Environmental Science and Pollution Research.* **2019**, *26(25)*, 25969–25984. https://doi.org/10.1007/s11356-019-05722-w.
5. Colombo, A.; Módenes, A.N.; Góes Trigueros, D.E.; Giordani da Costa, S.I.; Borba, F.H.; Espinoza-Quiñones, F.R. Treatment of Sanitary Landfill Leachate by the Combination of Photo-Fenton and Biological Processes. *Journal of Cleaner Production.* **2019**, *214*, 145–153. https://doi.org/10.1016/j.jclepro.2018.12.310.
6. Louhıchı, G.; Bousselmı, L.; Ghrabı, A.; Khounı, I. Process Optimization via Response Surface Methodology in the Physico-Chemical Treatment of Vegetable Oil Refinery Wastewater. *Environmental Science and Pollution Research.* **2019**, *26(19)*, 18993–19011. https://doi.org/10.1007/s11356-018-2657-z.
7. Cordier, C.; Charpin, L.; Stavrakakis, C.; Papin, M.; Guyomard, K.; Sauvade, P.; Coelho, F.; Moulin, P. Ultrafiltration: A Solution to Recycle the Breeding Waters in Shellfish Production. *Aquaculture*. **2019**, *504*, 30–38. https://doi.org/10.1016/j.aquaculture.2019.01.045.
8. Alonso, J.J.S.; El Kori, N.; Melián-Martel, N.; Del Río-Gamero, B. Removal of Ciprofloxacin from Seawater by Reverse Osmosis. *Journal of Environmental Management.* **2018**, *217*, 337–345. https://doi.org/10.1016/j.jenvman.2018.03.108.
9. Al-Karawi, A.J.M.; Al-Qaisi, Z.H.J.; Abdullah, H.I.; Al-Mokaram, A.M.A.; Al-Heetimi, D.T.A. Synthesis, Characterization of Acrylamide Grafted Chitosan and Its Use in Removal of Copper(II)

Ions from Water. *Carbohydrate Polymers*. **2011**, *83(2)*, 495–500. Doi: https://doi.org/10.1016/j.carbpol.2010.08.017.

10. Mustafa, H.J.; Al-Saadi, T.M. Study of Pb Ions Removal from Aqueous Solutions by a Novel Sodium Formate-Coated Magnetite Nanoparticles. *Journal of Physics: Conference Series*. **2021**, *1879*.https://doi.org/10.1088/1742-6596/1879/3/032112.
11. Muhi-Alden, Y.Y.; Saleh, K.A. Removing of Methylene Blue Dye from Its Aqueous Solutions Using Polyacrylonitrile/Iron Oxide/Graphene Oxide. *Iraqi Journal Science*. **2022**, *63(6)*, 2320–2330. https://doi.org/10.24996/ijs.2022.63.6.1.
12. Zhang, X.; Zhang, P.; Wu, Z.; Zhang, L.; Zeng, G.; Zhou, C. Adsorption of Methylene Blue onto Humic Acid-Coated Fe_3O_4 Nanoparticles. *Colloids and Surfaces A: Physicochemical and Engineering Aspects*. **2013**, *435*, 85–90. https://doi.org/10.1016/j.colsurfa.2012.12.056.
13. Tan, K.B.; Vakili, M.; Horri, B.A.; Poh, P.E.; Abdullah, A.Z.;Salamatinia, B. Adsorption of dyes by nanomaterials: recent developments and adsorption mechanisms. *Separation and purification technology*, **2015**, *150*, 229-242. https://doi.org/10.1016/j.seppur.2015.07.009.
14. Chaba, J.M.; Nomngongo, P.N. Effective Adsorptive Removal of Amoxicillin from Aqueous Solutions and Wastewater Samples Using Zinc Oxide Coated Carbon Nanofiber Composite. *Emerging Contaminants*. **2019**, *5*, 143–149. https://doi.org/10.1016/j.emcon.2019.04.001.
15. Li, J.; Xiong, S.; Liu, Y.; Ju, Z.; Qian, Y. High Electrochemical Performance of Monodisperse $NiCo_2O_4$ Mesoporous Microspheres as an Anode Material for Li-Ion Batteries. *ACS Appl. Mater. Interfaces* **2013**, *5(3)*, 981–988. https://doi.org/10.1021/am3026294.
16. Wu, X.; Wang, W.; Li, F.; Khaimanov, S.; Tsidaeva, N.; Lahoubi, M. PEG-Assisted Hydrothermal Synthesis of $CoFe_2O_4$ Nanoparticles with Enhanced Selective Adsorption Properties for Different Dyes. *Applied Surface Science*. **2016**, *389(10)*, 1003–1011. https://doi.org/10.1016/j.apsusc.2016.08.053.
17. Nezamzadeh-Ejhieh, A.; Shams-Ghahfarokhi, Z. Photodegradation of Methyl Green by Nickel-Dimethylglyoxime/ZSM-5 Zeolite as a Heterogeneous Catalyst. *Journal of Chemistry*. **2013**, *2013(1)*, 1-12. https://doi.org/10.1155/2013/104093.
18. Imranullah, M.; Hussain, T.; Ahmad, R.; Hwang, J.S.; Ahmad, S.; Shakir, I.; Kang, D.J. Hierarchical Porous Spinel Nickel Cobaltite Nanoflakes Anchored Reduced Graphene Oxide Nano-Photocatalyst for Efficient Degradation of Organic Pollutants under Natural Sunlight. *Journal of Materials Research and Technology*. **2021**, *15*, 623–632. https://doi.org/10.1016/j.jmrt.2021.08.030.
19. Faisal, A.A.H.; Abdul-Kareem, M.B.; Mohammed, A.K.; Ghfar, A.A. Novel Sorbent of Sand Coated with Humic Acid-Iron Oxide Nanoparticles for Elimination of Copper and Cadmium Ions from Contaminated Water. *Journal of Polymers and the Environment*. **2021**, *29(66)*, 3618–3635. https://doi.org/10.1007/s10924-021-02132-3.
20. Zhai, Y.; Mao, H.; Liu, P.; Ren, X.; Xu, L.; Qian, Y. Facile Fabrication of Hierarchical Porous Rose-like $NiCo_2O_4$ Nanoflake/MnCo2O4 Nanoparticle Composites with Enhanced Electrochemical Performance for Energy Storage. *Journal of Materials Chemistry A*. **2015**, *3*, 16142–16149. https://doi.org/10.1039/c5ta03017j.
21. Haripriya, M.; Sivasubramanian, R.; Ashok, A.M.; Hussain, S.; Amarendra, G. Hydrothermal Synthesis of $NiCo_2O_4$–NiO Nanorods for High Performance Supercapacitors. *Journal of Materials Science: Materials in Electronics*. **2019**, *30(8)*. https://doi.org/10.1007/s10854-019-01063-z.
22. Liu, M.-C.; Kong, L.-B.; Lu, C.; Li, X.-M.; Luo, Y.-C.; Kang, L.; Li, X.; Walsh, F.C. A Sol-Gel Process for the Synthesis of $NiCo_2O_4$ Having Improved Specific Capacitance and Cycle Stability for Electrochemical Capacitors . *Journal of The Electrochemical Society*. **2012**, *159*(8), A1262–A1266. https://doi.org/10.1149/2.057208jes.
23. Khalid, S.; Cao, C.; Wang, L.; Zhu, Y. Microwave Assisted Synthesis of Porous $NiCo_2O_4$ Microspheres: Application as High Performance Asymmetric and Symmetric Supercapacitors with Large Areal Capacitance. *Scientific Reports*. **2016**, *6(1)*, 1-13. https://doi.org/10.1038/srep22699.
24. Tian, Y.; Li, H.; Ruan, Z.; Cui, G.; Yan, S. Synthesis of $NiCo_2O_4$ Nanostructures with Different

Morphologies for the Removal of Methyl Orange. *Applied Surface Science*. **2017**, *393*, 434–440. https://doi.org/10.1016/j.apsusc.2016.10.053.

25. Guan, X.; Luo, P.; Yu, Y.; Li, X.; Chen, D. Solvent-Tuned Synthesis of Mesoporous Nickel Cobaltite Nanostructures and Their Catalytic Properties. *Applied Sciences*. **2019**, *9(6)*, 1100. https://doi.org/10.3390/app9061100.
26. Adeyemo, A.A.; Adeoye, I.O.; Bello, O.S. Adsorption of Dyes Using Different Types of Clay: A Review. *Applied Water Science*. **2017**, *7*, 543–568. https://doi.rg/10.1007/s13201-015-0322-y.
27. Khudhaier, S.R.; Awad, A.A.; Al-Heetimi, D.T.A.; Al-Karawi, A.J.M.; Al-Kinani, E.M.; Omarali, A.A.B.; Al-Qaisi, Z.H.J.; Khalaf, Q.Z. Synthesis of Chitosan–Iron Keplerate Composite as an Adsorbent for Removal of Toxic Ions from Water. *Desalin. Water Treat.* **2019**, *157*, 165–176. https://doi.org/10.5004/dwt.2019.24157.
28. Atiya, M.A.; Hassan, A.K.; Kadhim, F.Q. Green Synthesis of Copper Nanoparticles Using Tea Leaves Extract to Remove Ciprofloxacin (CIP) from Aqueous Media. *Iraqi Journal Science*. **2021**, *62*(9), 2833–2854. https://doi.org/10.24996/ijs.2021.62.9.1.
29. Abbas, A.M.; Merza, S.H. Preparation and Characterization of Graphene Oxide - Attapulgite Composite and Its Use in Kinetic Study of Alizarin Dye Adsorption from Aqueous Media. *Egyptian Journal of Chemistry*. **2020**, *63(2)*, 561–572. https://doi.org/10.21608/ejchem.2019.15600.1946.
30. Bahgat, M.; Farghali, A.A.; El Rouby, W.; Khedr, M.; Mohassab-Ahmed, M.Y. Adsorption of Methyl Green Dye onto Multi-Walled Carbon Nanotubes Decorated with Ni Nanoferrite. *Applied Nanoscience*. **2013**, *3*(3), 1–11. https://doi.org/10.1007/s13204-012-0127-3.
31. Farghali, A.A.; Bahgat, M.; El Rouby, W.M.A.; Khedr, M.H. Preparation, Decoration and Characterization of Graphene Sheets for Methyl Green Adsorption. *Journal of Alloys and Compounds*. **2013**, *555*, 193–200. https://doi.org/10.1016/j.jallcom.2012.11.190.
32. Wang, J.; Guo, X. Adsorption Kinetic Models: Physical Meanings, Applications, and Solving Methods. *Journal of Hazardous Materials*. **2020**, *390*, 122156. https://doi.org/10.1016/j.jhazmat.2020.122156.
33. Pholosi, A.; Naidoo, E.B.; Ofomaja, A.E. Intraparticle Diffusion of Cr(VI) through Biomass and Magnetite Coated Biomass: A Comparative Kinetic and Diffusion Study. *South African Journal of Chemical Engineering*. **2020**, *32*, 39–55. https://doi.org/10.1016/j.sajce.2020.01.005.
34. Body, G.E.; Adamson, A.W.; Myers Jr, L.S. The Exchange Adsorption of Ions from Aqueous Solutions by Organic Zeolites. 11. Kinetics. In *Chemical Engineering Journal* **1947**, *69(11)*, 2836–1948. https://doi.org/10.1021/ja01203a066.
35. Karaoğlu, M.H.; Zor, Ş.; Uğurlu, M. Biosorption of Cr(III) from Solutions Using Vineyard Pruning Waste. *Chemical Engineering Journal*. **2010**, *159(1-3)*, 98–106. https://doi.org/10.1016/j.cej.2010.02.047.
36. Abbas, A.M.; Abd, S.S.; Himdan, T. abdulhadi Kinetic Study of Methyl Green Dye Adsorption from Aqueous Solution by Bauxite Clay at Different Temperatures. *Ibn AL-Haitham Journal For Pure and Applied Science*. **2018**, *31*(1), 58–66. http://doi.org/10.30526/31.1.1853.
37. Bengar, S.A.; Zanjanchi, M.A.; Sohrabnezhad, S. Adsorptive Characteristics and Performance of Template-Containing Mcm-41 for Removal of Sodium Dodecylbenzene Sulfonate from Aqueous Solutions. *Desalination and Water Treatment*. **2021**, *212*, 415–427. https://doi.org/10.5004/dwt.2021.26601.
38. Mohammed, F.F. Equilibrium, Kinetic, and Thermodynamic Study of Removing Methyl Orange Dye from Aqueous Solution Using Zizphus Spina-Christi Leaf Powder. *Baghdad Science Journal*. **2022**, *20*(*2*), 0296. https://doi.org/10.21123/bsj.2022.7036.